Two-color polarization control of angularly resolved attosecond time delays

D. I. R. Boll [*]
Instituto de Física Rosario, CONICET-UNR, Ocampo y Esmeralda, 2000 Rosario, Santa Fe, Argentina

L. Martini
Instituto de Física Rosario, CONICET-UNR, Ocampo y Esmeralda, 2000 Rosario, Santa Fe, Argentina
and Department of Physics and Astronomy, University of Southern California, Los Angeles, California 90089-0484, USA

A. Palacios
Departamento de Química, Módulo 13, Universidad Autónoma de Madrid, 28049 Madrid, Spain
and Institute of Advanced Research in Chemical Sciences, Universidad Autónoma de Madrid, 28049 Madrid, Spain

O. A. Fojón
Instituto de Física Rosario, CONICET-UNR, Ocampo y Esmeralda, 2000 Rosario, Argentina
and Escuela de Ciencias Exactas y Naturales, FCEIA, Universidad Nacional de Rosario, 2000 Rosario, Santa Fe, Argentina

(Received 29 December 2022; accepted 27 March 2023; published 12 April 2023)

Measured photoionization time delays may exhibit large variations as a function of the emission angles, even for spherically symmetric targets, as shown in recent reconstruction of attosecond beating by interference of two-photon transitions (RABBITT) experiments. The contributions from different pathways to the two-photon quantum channels can explain the observed phase jumps that shape those angular distributions. Here we propose a simple analytical model to describe angularly resolved RABBITT spectra as a function of the relative polarization angle between the ionizing attosecond pulse train and the assisting IR field. We demonstrate that the angular dependences of the measured delays can be analytically predicted and the position of the phase jumps reduced to the analysis of a few relevant parameters.

DOI: 10.1103/PhysRevA.107.043113

I. INTRODUCTION

The chronoscopy of electron photoemission [1] turned into reality upon the mastery of two pump-probe attosecond spectroscopy techniques: attosecond streaking [2] and reconstruction of attosecond beating by interference of two-photon transitions (RABBITT) [3,4]. While originated as characterization procedures for attosecond pulses, they have become the most successful experimental approaches to access the so-called Eisenbud-Wigner-Smith (EWS) time delays for single-photon ionization processes [1,5–8]. The EWS photoionization time delay holds information on the initial state and the potential experienced by the electron while escaping. Thus, it conveys rich structural and dynamical information on the potential landscape where electrons evolve. Accordingly, the EWS time delay will depend on photoelectron energy and its emission direction unless a single partial wave in the continuum prevails [1,5,9,10].

The retrieval of EWS time delays from attosecond spectroscopic experiments requires a careful examination of the effects induced by the probe field [11,12]. The frequency spectrum of typical attosecond pulse trains in RABBITT experiments comprises a comb of extreme ultraviolet (XUV) odd-order harmonics from a fundamental infrared (IR) laser, giving rise to photoelectron main bands. Consequently, the ionization of a target with an attosecond pulse train assisted with a phase-locked IR laser leads to another set of photoelectron spectral lines (sidebands), which lie in between the main bands and correspond to the interfering two-photon (XUV ± IR) channels. This interference leads to a pump-probe delay (τ) -dependent signal in the sideband that follows the expression [4]

$$I_{2q}(\tau) \propto A + B\cos(2\omega_0\tau - \phi_{\mathrm{at}}), \tag{1}$$

where ω_0 is the IR photon frequency and ϕ_{at} $(=2\omega_0\tau_{\mathrm{at}})$ is the phase difference that carries the total photoelectron emission delay τ_{at}, which results from the EWS and the measurement-induced continuum-continuum time delays [12].

Previous studies established that total atomic delays usually follow the additive relation $\tau_{\mathrm{at}} = \tau_{\mathrm{EWS}} + \tau_{\mathrm{cc}}$ for atomic targets in nonresonant angle-integrated measurements [8,13,14]. However, the lack of spherical symmetry prevents finding a direct connection between total and EWS time delays in molecular targets [15,16]. The situation is much more challenging in angle-resolved measurements [17–24]. In that case, angular dependences induced on the IR probing stage may be the primary source of measured time-delay anisotropies. Indeed, for initial *s* states in atomic systems, the EWS time delay is strictly angle independent, whereas the

---

[*] boll@ifir-conicet.gov.ar

©2023 American Physical Society

total time delays retrieved from RABBITT experiments display steep variations for some emission angles [17]. These angular variations, attributed to small phase differences induced on the continuum-continuum transitions [17], are also explained by destructive interferences on the absorption channel, governed by the relative weight of partial waves populated by the IR field [19].

The angular dependences of total time delays arising on RABBITT experiments are customarily described through numerical methods. Here we show that a simplified analytic model for the two-photon matrix elements can accurately describe the angular variations of time delays, particularly those induced by the IR probe. To that end, we consider the total time delay for initial s states in atomic systems and compare it with available experimental data [17]. Then we resort to the polarization control technique [25,26] to externally manipulate the relative weight of partial waves. In that case, the angular evolution of time delays displays marked differences [27]. We show that an interference mechanism, latent in the parallel case, is coresponsible for the observed total time-delay variations in that scenario.

II. THEORETICAL METHODS

The angular variation of atomic time delays is intrinsically linked with the photoelectron angular distributions (PADs) [17,19,28–30]. The most general expression for PADs is given by [31]

$$I_{2q}(\theta,\phi) \propto \left| \sum_{L,M} M_{L,M} Y_L^M(\theta,\phi) \right|^2, \tag{2}$$

where θ and ϕ are the angles defining the electron emission direction and Y_L^M is a spherical harmonic function. The method of partial waves, implicit in the equation above, allows us to obtain a convenient expression of the transition matrix amplitudes $M_{L,M}$ [32] that connect the initial bound state of the atomic target with a final continuum state, labeled by the azimuthal and magnetic quantum numbers L and M, respectively.

In the RABBITT spectra, the time-delay information emerges in the sidebands [8,12]. The quantum pathways involving the absorption (+) or emission (−) of an IR photon from consecutive odd harmonics add coherently. The transition matrix element can then be formally separated into two terms

$$M_{L,M} = M_{L,M}^{+} + M_{L,M}^{-} \tag{3}$$

that collect the contributions to each channel. For typical IR intensities in RABBITT experiments, the analysis of $M_{L,M}^{\pm}$ can be carried out through second-order perturbation theory (SOPT). In the limit of infinitely long pulses, each transition matrix amplitude reads

$$M_{L,M}^{\pm} = e^{\pm i\omega_0\tau} \sum_{\lambda,\mu} A_{L,\lambda,l_i}^{M,\mu,m_i} T_{L,\lambda}^{l_i,\pm}. \tag{4}$$

The summation above runs over the azimuthal (λ) and magnetic (μ) quantum numbers of intermediate states allowed by the application of the electric dipole selection rule from the initial state with angular quantum numbers l_i and m_i. The angular factors $A_{L,\lambda,l_i}^{M,\mu,m_i}$ are identical for absorption and emission channels, but the radial matrix elements $T_{L,\lambda}^{l_i,\pm}$, in general, are not [17,19,33].

In the two-color case, the latter splits into the sum of two terms

$$T_{L,\lambda}^{l_i,\pm} = T_{L,\lambda}^{l_i}(\Omega_{\mp}) + T_{L,\lambda}^{l_i}(\pm\omega_0), \tag{5}$$

describing the possible time orderings for the two-photon processes that lead to the same final continuum state. The first term accounts for the absorption of one XUV photon with frequency $\Omega_{\mp} = (2q \mp 1)\omega_0$ from the attosecond pulse train and the subsequent absorption (+) or emission (−) of one IR photon. The other term describes the reverse process where the exchange of one IR photon is followed by the absorption of the XUV photon. In the length gauge, each term on the right-hand side of Eq. (5) reads

$$T_{L,\lambda}^{l_i}(\Omega) = (-i)^L e^{i\sigma_L} \sum\!\!\!\!\!\!\!\int \frac{\langle R_{\varepsilon_{k_e},L}|r|R_{\varepsilon_\kappa,\lambda}\rangle\langle R_{\varepsilon_\kappa,\lambda}|r|R_{\varepsilon_i,l_i}\rangle}{\varepsilon_i + \Omega - \varepsilon_\kappa}, \tag{6}$$

where $\sigma_L = \arg\Gamma(L + 1 - i/k_e)$ is the Coulomb phase for a final state with angular momentum L and momentum k_e. The summation (integration) runs over the entire spectrum of unperturbed states of the target, with energy ε_κ and radial wave functions $R_{\varepsilon_\kappa,\lambda}$. The initial and final states of the system are also described by eigenstates of the field-free Hamiltonian, with radial wave function R_{ε_i,l_i} and $R_{\varepsilon_{k_e},L}$, respectively [33].

To highlight the influence of the continuum-continuum transitions on the angular variation of atomic time delays, we focus on initial s ($l_i = 0$) states. In turn, this initial-state configuration will allow us to directly compare the results of our model with benchmark experimental and theoretical data [17,19,28]. Figure 1(a) schematically displays the most relevant reaction pathways contributing to a generic sideband of order $2q$. As the angular momentum of every intermediate state is $\lambda = 1$, we can drop the indices l_i and λ to simplify notation. Substituting Eq. (3) into Eq. (2) and expanding it with the use of Eq. (4), we obtain a series whose terms can be classified into two categories based on their explicit dependence on $\omega_0\tau$.

On the one hand, nonoscillatory terms are independent of τ and we can group them into a variable customarily termed A (or α) [12,28]. On the other hand, we may combine the oscillatory terms into the double series

$$\sum_{L,L'} |T_L^+||T_{L'}^-| g_{L,L'} \cos(2\omega_0\tau + \phi_L^+ - \phi_{L'}^-), \tag{7}$$

where $|T_L^{\pm}|$ and $\phi_L^{\pm}$ are the moduli and phase of the radial matrix element in Eq. (5), for absorption and emission pathways. The function $g_{L,L'}$ contains the full angular information. To obtain the explicit expressions for $g_{L,L'}$ (see the Appendix) we adopt the geometric layout presented in Fig. 1(b). We choose the quantization axis for angular momentum in the z direction, whereas the attosecond pulse train is linearly polarized (blue vector) along the x axis. The polarization vector of the IR laser (red vector) and the photoelectron emission direction (green vector) lie in the xy plane subtending the angles Θ and θ with respect to the x axis, respectively.

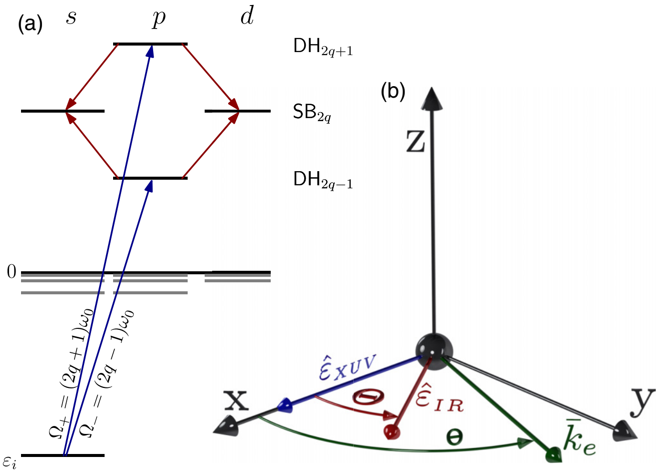

FIG. 1. (a) Schematic representation of pathways contributing to consecutive main bands and the sideband in between. For low IR intensities, main bands are mainly populated by transitions from the ground state to continuum states, triggered by the absorption of a single photon with energy $\Omega_\pm = (2q \pm 1)\omega_0$, from the attosecond pulse train. The interaction of these primary photoelectron distributions with the IR gives rise to the sidebands. The reverse contributions, where the IR photon is absorbed or emitted first, are not shown here. (b) Geometric configuration. We indicate the polarization direction of the XUV laser source by the blue vector $\hat{\varepsilon}_{\mathrm{XUV}}$ collinear to the Cartesian x axis. The polarization vector of the IR laser $\hat{\varepsilon}_{\mathrm{IR}}$ lies in the xy plane and subtends an angle Θ with the Cartesian x axis. The final photoelectron momentum also lies in the xy plane and it is indicated by the green vector $\mathbf{k}_e$.

The series above can be summed to give $B\cos(2\omega_0\tau - \phi_{\mathrm{at}})$ by virtue of the harmonic addition theorem [34]. Thus, the photoelectron angular distributions of sideband lines reduce to Eq. (1) also for angle-resolved setups. The angular dependence is entirely contained in factors A, B, and the atomic phase ϕ_{at} that satisfies the equation

$$\tan(\phi_{\mathrm{at}}) = \frac{\sum_{L,L'} |T_L^+||T_{L'}^-|g_{L,L'} \sin(\phi_{L'}^- - \phi_L^+)}{\sum_{L,L'} |T_L^+||T_{L'}^-|g_{L,L'} \cos(\phi_{L'}^- - \phi_L^+)}. \tag{8}$$

This atomic phase ϕ_{at} is connected to the so-called total atomic delay by $\tau_{\mathrm{at}} = \phi_{\mathrm{at}}/2\omega_0$ [17] because we consider Fourier limited (chirp-free) attosecond pulses in the train [28].

From Eq. (8) we can unambiguously identify a necessary condition to observe angular variations in time delays: The phase of the radial matrix elements must depend on the angular quantum number of the final state. Otherwise, if $\phi_L^\pm = \phi^\pm$, the trigonometric functions on the right-hand side of Eq. (8) can be factorized, the contribution of the $g_{L,L'}$ functions cancels identically, and the angular dependence on ϕ_{at} is completely lost.

One main contribution of this paper is to show that a purely analytic method can quantitatively describe the angular variation of atomic time delays, even for multielectronic targets. Starting from Eq. (8) and based on the condition established in the preceding paragraph, we must resort to a model capturing the dependence of radial matrix elements on the angular quantum numbers of final states. The analytic continuum-continuum radial matrix elements (ACC-RME) model [33] meets these requirements. Additionally, our model allows for a factorization of radial matrix elements as

$$T_L^\pm = |T_L^\pm| e^{i\phi_L^\pm} \simeq |T_{L,bc}^\pm||T_{L,cc}^\pm| e^{i(\phi_{bc}^\pm + \phi_{L,cc}^\pm)}, \tag{9}$$

where $T_{L,bc}^\pm$ describes the ionization step of the reaction and $T_{L,cc}^\pm$ accounts for transitions upon exchange of one IR photon. This feature is common to most, if not all, of the procedures to model radial matrix elements and it is the key to accessing the EWS time delay from RABBITT [12] (or streaking [11]) traces. The added value of the ACC-RME model is that $T_{L,cc}^\pm$ factors depend on the angular quantum number of final states, in contrast to previous analytic approaches [12]. That aspect of our model allows us to survey the angular variation of total atomic delays from a fully analytical perspective. In addition, the ACC-RME model satisfactorily recovers the universal character observed for the phases and moduli of continuum-continuum transitions [19,30]. Thus, provided reactions develop in spectral regions with smooth background continua and multielectron effects [18,35,36] are negligible, the study of general features of two-color angularly resolved total atomic time delays for initial s states can be constrained to hydrogenlike targets without loss of generality. We further test the validity and accuracy of the model by comparing it with available experimental data, the results from the numerical solution of the time-dependent Schrödinger equation (TDSE), and the widely employed SOPT.

III. RESULTS

We obtain the angle-resolved RABBITT spectra by solving the TDSE with the QPROP code [37] for a comb of odd harmonics with orders 11–27 and different pump-probe delays τ. We consider cosine-squared envelopes for both the XUV and IR radiation fields, with three and ten IR cycles of total duration, respectively. To ensure that the system remains within the perturbative regime, we set the intensity of the 800-nm ($\omega_0 = 1.55$ eV) IR field to 5×10^{10} W/cm^2. We extract the total atomic time delay by fitting to Eq. (1) the sideband signal dependence on τ. Additionally, we substitute into Eq. (8) the radial matrix elements we obtain from SOPT [38] and ACC-RME [33] methods. First, we revisit the case of collinear polarization of pump-and-probe fields for which theoretical and experimental benchmark data are available [17,19,28]. Then we explore the noncollinear case. Data sets for the atomic time delays we obtain through all these methods and for each configuration are publicly available [39]. Atomic units are used unless stated otherwise.

A. Parallel case $\Theta = 0°$

From a theoretical point of view, we can provide precise values for the photoemission time delay. However, the experimental determination of this quantity employs attosecond pulse trains, usually generated with a frequency chirp that is difficult to retrieve. Thus, it is common to extract relative time delays with respect to a given reference. This is straightforward for angularly resolved measurements since there is a perfect cancellation of the XUV phase when using as a reference the signal retrieved for a specific angle.

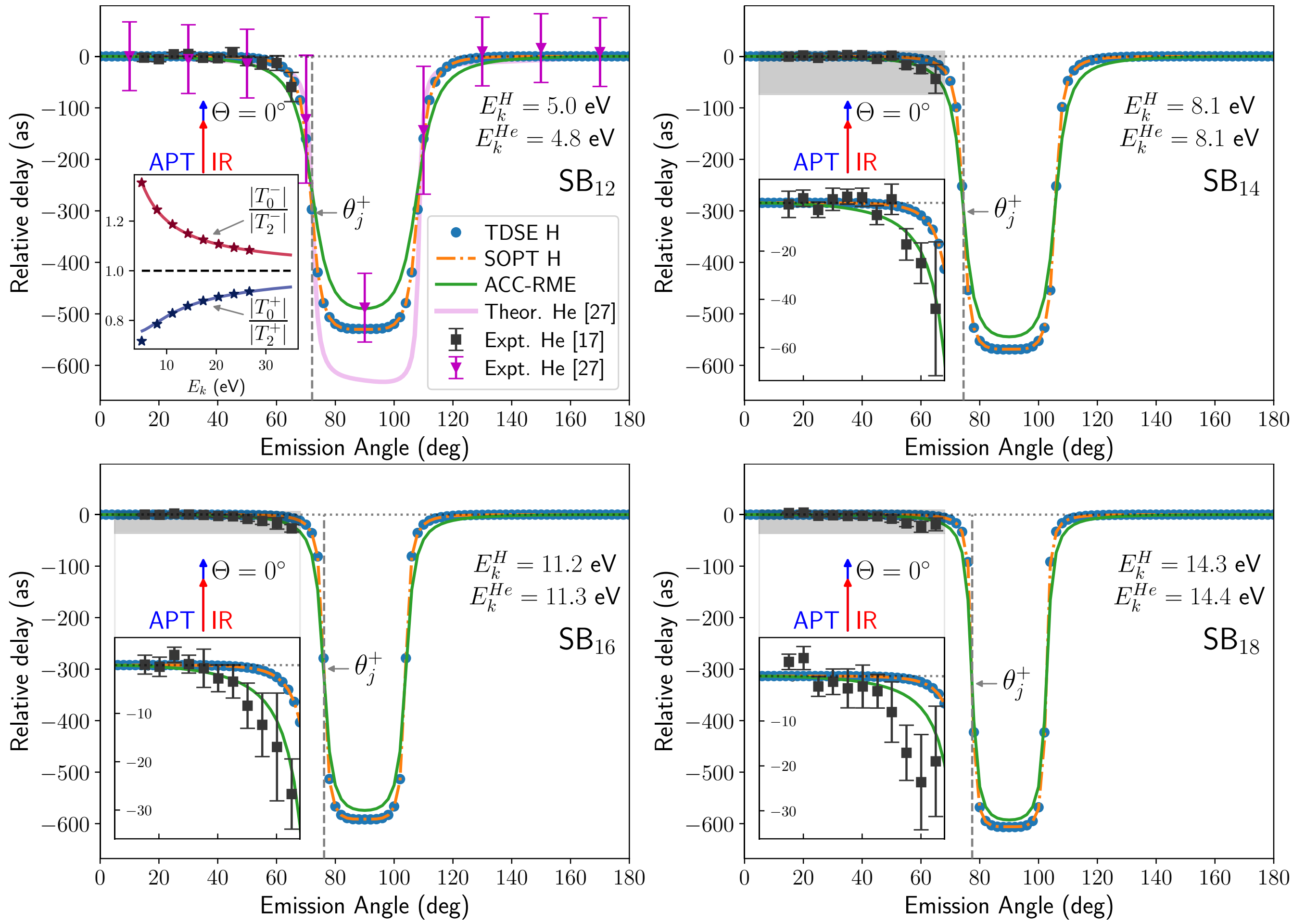

FIG. 2. Comparison of the angular variation of time delays at photoelectron energies coinciding with RABBITT sidebands for hydrogen and helium atoms. Theoretical calculations for the hydrogen atom are computed through three different methods: TDSE, SOPT, and ACC-RME calculations. The data from Refs. [17,27] correspond to the helium atom. The photoelectron kinetic energy of final states in both systems are indicated in each panel. The sideband index corresponds to hydrogen. The phase jump angle θ_j^+ is calculated from Eq. (11) and the relative time delay for that emission angle is obtained from linear interpolation from the TDSE results. This leads to larger fluctuations for sidebands with larger index due to the steeper variations of $\Delta\tau_{\text{tot}}$. The inset in figure for SB$_{12}$ shows the ratios $|T_0^{\pm}/T_2^{\pm}|$ obtained from SOPT (stars) and ACC-RME (lines) calculations [33]. The other insets show the close-up image of relative time delays for the gray-shaded areas.

In Fig. 2 we present the angularly resolved total time delays for the hydrogen atom in the standard RABBITT scheme, i.e., with a parallel linearly polarized XUV attosecond pulse train and IR field. We display the relative time delays, considering as reference the value for photoelectron emission parallel to the light polarization direction $\Delta\tau_{\text{at}}(\theta) = \tau_{\text{at}}(\theta) - \tau_{\text{at}}(0°)$. The results correspond to sidebands 12–18 in hydrogen, initially in its ground state. Model predictions (green solid line) agree with *ab initio* results obtained within the SOPT (orange dashed line) and by solving the TDSE (blue circles). We observe that the mean-squared error of model results with respect to those from *ab initio* calculations decreases as the photoelectron kinetic energy increases. Slight inaccuracies in the phase of each radial matrix element derived from the ACC-RME model explain the differences from the *ab initio* calculations. In contrast, the moduli (quotient) of ACC-RME radial matrix elements are in almost perfect agreement with state-of-the-art calculations, as the inset in the figure for SB$_{12}$ reveals. For comparison, we also include the experimental data for the He atom from Ref. [17]. It is interesting to note that, except for sideband 12, ACC-RME results better describe the experimental data (see insets for sidebands 14–18). This seems to be a fortuitous circumstance. The model provides slightly larger (smaller) phase differences between partial waves s and d in the absorption (emission) channels compared to accurate calculations [33]. In turn, these shifts seem to reproduce the spectral contamination effect that pervades the experimental data [17].

The relative time delay presents steep variations for electron emission angles θ above 65°, as discussed in previous studies [17,19,28]. In the past, the analysis of this trend focused on the spherical harmonics describing the angular dependence of photoemission [17] and their interplay with the transition matrix amplitudes [19]. Here we present an alternative procedure for studying the phase jumps in atomic time delay using simple analytical expression. We start from the definition of relative time delays $\Delta\tau_{\text{at}}(\theta)$ and combine it with the expression for atomic phases in Eq. (8). The angular dependence of relative time delays reduces to

$$\Delta\tau_{\mathrm{tot}}(\theta) = \frac{1}{2\omega_0}\arctan\left(\frac{f(\theta) - f(0)}{1 + f(\theta)f(0)}\right), \tag{10}$$

where $f(\theta)$ is the right-hand side of Eq. (8). Phase jumps will occur for zero values of the denominator in the arctan function argument. However, in order to reach a simplified analytical expression to predict the phase jumps, we will consider the very likely scenario in which the phase differences between different partial waves are almost equal for absorption and stimulated emission [30,33], or equivalently $\phi_0^{\pm} \simeq \phi_2^{\pm} + \Delta$, with $|\Delta| \ll 1$. Applying this approximation and for $\Delta = 0$,[1] we obtain a quadratic equation in $\cos(2\theta)$ for the phase jump angles that satisfies the relation

$$\cos(2\theta_j^{\pm}) \simeq -\left(\frac{1}{3} + \frac{2}{3}\frac{|T_0^{\pm}|}{|T_2^{\pm}|}\right). \tag{11}$$

Here we remark that $\Delta \neq 0$ is a necessary condition for the obtention of atomic time delays depending on the photoelectron emission angle. Otherwise, $f(\theta) \equiv f(0)$ in Eq. (10) and no phase jump can occur because the angular dependenc is lost. However, the specific values of Δ do not influence the position of phase jump angles $\theta_j^{\pm}$ as long as $|\Delta| \ll 1$.

From Eq. (11) we see that the modulus quotient of radial matrix elements $T_L^{\pm}$ largely dictates the photoelectron emission angles where phase jumps take place. Even though propensity rules are liable to be overridden at some specific conditions [40,41], we find that the qualitative usefulness of Eq. (11) improves by combining it with the generalized Fano propensity rule [19]. It states that continuum-continuum transitions triggered by the absorption (emission) of one IR photon favor the partial wave with higher (lower) angular momentum. Thus, phase jumps shown in Fig. 2 can only result from absorption pathways, as the quotient satisfies $0 < |T_0^{+}/T_2^{+}| \leqslant 1$, and we can always find a real solution θ_j^{+} to Eq. (11). The vertical dashed lines in Fig. 2 display the phase jump angles θ_j^{+} we obtain by using radial matrix elements from SOPT calculations [33,38]. Conversely, emission channels cannot induce phase jumps on this setup. The inset in Fig. 2 for SB_{12} quantitatively depicts the generalized Fano propensity rule for initial s states. The almost perfect agreement between exact SOPT (stars) and ACC-RME model (solid lines) results over the entire energy range illustrates the accuracy of the analytic method when it comes to predicting modulus ratios of radial matrix elements. Consequently, we can safely invoke the factorization of radial matrix elements that the ACC-RME model predicts to reach an additional conclusion. The phase jump angle θ_j^{+} derived from Eq. (11) will only depend on the relative strength of the continuum-continuum transitions $p \rightarrow s$ and $p \rightarrow d$. Ultimately, this allows us to conjecture a direct dependence of the phase jump angles on the photoelectron energy, the net charge of the parent ion, and the IR photon wavelength.

For comparison, in Fig. 2 we also include the experimental data for the relative total atomic delays in helium reported in Ref. [17]. The similarity between the theoretical results for hydrogen and the experimental data for helium is not surprising and follows from two facts. First, the single-electron dynamics dominates the response of helium atoms in this energy range [17,40]. Second, the quotients of transition matrix amplitudes for s and d partial waves, $T_0^{\pm}/T_2^{\pm}$, govern the relative time-delay patterns [17]. Moreover, as the moduli and phases of these quotients follow a universal pattern for the same final photoelectron energy [19,30,33], the angular variation of time delays for hydrogen and helium atoms must be similar. The assertion above is further tested by recent experimental results [27]. Although the measurement was conducted using a stronger IR field, our theoretical results fall within the error bounds of the observations. To appraise the impact of stronger IR fields on angular variations of time delays, we perform an additional set of TDSE simulations, using IR intensities around the experimental value. The results we obtain for total atomic delays using a stronger IR intensity (not shown here) are almost identical to those in the perturbative regime. Therefore, we can discard the IR intensity as the (only) source for the asymmetry displayed by the theoretical data in Ref. [27] and reproduced in Fig. 2. Moreover, the agreement of our results for low and high IR intensities allows us, in principle, to rule out focal volume averaging effects on this observable.

This universal trend is also captured in the results plotted in Fig. 2, where we specify the photoelectron energy in each sideband for both hydrogen and helium targets. For other initial states, bound-continuum contributions may have a non-negligible role in defining the phase jump emission angles because intermediate states will have more than one possible angular momentum value.

B. Nonparallel case $\Theta \neq 0°$

In the following, we explore the angularly resolved phase differences (or equivalently in terms of time delays) resulting from RABBITT spectra for different relative polarization angles Θ between the attosecond pulse train and the IR field. In such a scheme, the light-atom system no longer has cylindrical symmetry and atomic time delays depend on both the azimuthal and polar emission angles. We focus on electron emission into the plane defined by the polarization vectors of the XUV and IR fields. From now on, θ denotes the photoelectron emission angle in the xy plane measured from the positive x axis, the polarization direction of the attosecond pulse train (see Fig. 1).

In Fig. 3 we depict the angular variation of atomic time delays for sidebands 12–16 in hydrogen and different relative polarization angles Θ between the XUV and IR fields. We notice that a double-well pattern unfolds as Θ increases. The broad symmetric valley shapes found for collinear fields (Fig. 2) become two narrow shapes at specific angles (Fig. 3). To reveal the physical origin of this phenomenon, we generalize the equation to obtain the approximate phase jump angles to the case of noncollinear laser polarization directions. Following the same steps leading to Eq. (11), we find that phase jump angles in the nonparallel case satisfy the relation

$$\cos(2\theta_j^{\pm} - \Theta) \simeq -\left(\frac{1}{3} + \frac{2}{3}\frac{|T_0^{\pm}|}{|T_2^{\pm}|}\right)\cos\Theta, \tag{12}$$

---

[1] The next-order term in the Taylor expansion around $\Delta = 0$ of the solutions to the quadratic equation are negligible due to $|\Delta| \ll 1$.

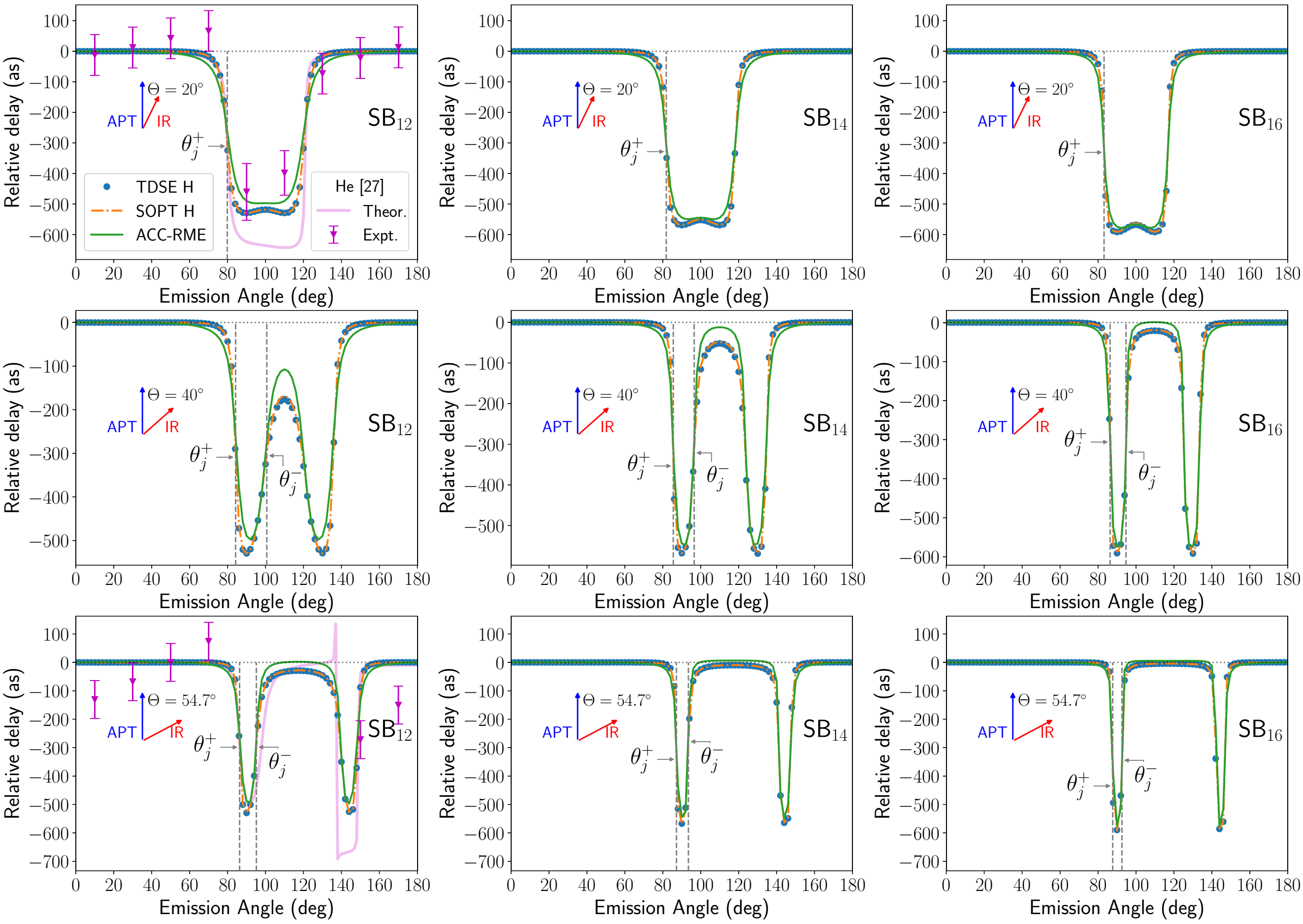

FIG. 3. Angularly resolved atomic time delays at photoelectron energies coinciding with RABBITT sidebands for hydrogen atoms and different relative polarization angles Θ. The results are computed through three different methods: TDSE, SOPT, and ACC-RME calculations. Theoretical and experimental data for helium were taken from Ref. [27]. The phase jump angles $\theta_j^{\pm}$ were obtained from Eq. (12) and the relative time delay for that emission angle was obtained from linear interpolation of the TDSE results. This procedure may lead to larger fluctuations for sidebands with larger index due to the steeper variation of $\Delta\tau_{\text{tot}}$. We display only the first occurrence of the phase jump angles $\theta_j^{\pm}$ associated with absorption and emission pathways. The second phase jump angle for each family arises at emission angles symmetric with respect to $(\pi + \Theta)/2$.

after setting $\Delta = 0$. A distinctive feature of this equation, and perhaps the central contribution of this paper, is that it predicts the emergence of another family of phase jump angles. Briefly, the $\cos\Theta$ factor can make the right-hand side greater than -1, regardless of the value for $|T_0^{\pm}/T_2^{\pm}|$. Therefore, it will be possible to find real solutions also for phase jump angles θ_j^{-}, associated with emission pathways, which are forbidden in the parallel case. The availability of a second family of phase jump angles should therefore restore atomic time delays to values similar to those found before the first phase jump induced by the absorption pathways. Hence, changing the relative polarization angle can split the broad time-delay valleys obtained for the parallel case into two narrower ones. For sidebands 12–16, we find that a relative polarization angle Θ larger than approximately 35° leads to physical solutions also for emission pathways, in agreement with the results in Fig. 3. Thus, the analytic expression in Eq. (12) predicts, in a simplified manner, all the phase jump angles that ultimately shape the angular evolution of atomic time delays.

As in the parallel case, the vertical dashed lines mark the phase jump angles we calculate from Eq. (12) using SOPT radial matrix elements. Although we do not explicitly indicate them, each family presents a second phase jump at emission angles symmetric with respect to $(\pi + \Theta)/2$. A visual inspection of Fig. 3 leads us to conclude that solutions $\theta_j^{\pm}$ provide a reasonable approximation for the full width at half minima of the time-delay valleys. Therefore, by using Eq. (12), we can analyze the narrowing of the time-delay valleys with increasing photoelectron energy or the relative polarization angle. For fixed Θ values, the quotient $|T_0^{+}/T_2^{+}|$ increases for increasing photoelectron energy, as the inset in Fig. 2 shows. In that case, the right-hand side of Eq. (12) will tend to $-\cos\Theta$ from above. In the asymptotic region, where $|T_0^{+}| \simeq |T_2^{+}|$, the first occurrence of the phase jump angle θ_j^{+} will approach 90° from the left, i.e., the phase jump will occur for electron emission perpendicular to the polarization vector of the attosecond pulse train. A similar analysis shows that the other phase jump enclosing the time-delay valley will approach 90° from the right.

The previous analysis shows the role that radial degrees of freedom play in shaping the angular variation of atomic time delays through the radial matrix elements. Alternatively, the angular degrees of freedom may induce similar effects. Larger tilt angles Θ may also cause a narrowing of the time-delay valleys we obtain for sidebands, as Fig. 3 shows. Under the assumption that photoelectron kinetic energy remains constant, larger Θ values make the right-hand side of Eq. (12) approach zero from below because of the $\cos\Theta$ factor. At first glance, this factor should push the phase jump angle θ_j^+ to the left. However, this effect is overcompensated by the $\Theta/2$ shift arising from the left-hand side of Eq. (12). In sum, increasing the tilt angle Θ has a net effect on the width of time-delay valleys similar to considering higher photoelectron kinetic energies. Here the angular algebra induces a depletion of s final continuum states when Θ values move towards 90°. This depletion is responsible for the better agreement between our model and *ab initio* results we observe for larger Θ values. From a qualitative point of view, this trend relates to the fact that models based on approximate wave functions for intermediate and final states are expected to perform better when phase differences between partial waves of final continuum states approach zero.

The results in Fig. 3 display two minima for the total time delay. One of them corresponds to electron emission perpendicular to the XUV polarization vector, as observed in the parallel case. The other one occurs for electron emission directions perpendicular to the IR polarization vector, irrespective of the tilt angle Θ and photoelectron kinetic energy. A recent theoretical and experimental study conducted on noble-gas atoms [27] reached the same conclusion about the latter minimum. For increasing relative polarization angles Θ, the comparison of our results with the experimental observations [27] deteriorates. The drift towards higher total time delays that observations for helium display contrasts with theoretical results, even those for larger IR intensities. On the other hand, the agreement of our results with theoretical data from Ref. [27] is more satisfactory. The largest discrepancies are observed for electron emission directions perpendicular to the IR polarization vector.

Low photoelectron emission probabilities usually hinder the direct observation of minima described above [17,27]. A more efficient approach to experimentally verify their existence is to induce on the system the double phase jumps we reveal. Contrary to what Fig. 3 might suggest, the emergence of the double-well structure is not restricted to tilt angles larger than 35°. The interplay of radial and angular degrees of freedom evidenced in Eq. (12) makes it possible to find that signature for every angle $\Theta \neq 0$ provided the photoelectron kinetic energy ε_{k_e} is high enough. Nonetheless, for asymptotically large ε_{k_e} values, the quotient of radial matrix elements approaches unity with the consequent decrease in the width of the wells, making them harder (if not impossible) to detect experimentally. Clearly, photoelectron emission probabilities play a central role in studying this phenomenon.

C. Photoelectron emission probabilities

Next we focus on how the relative polarization angle Θ modifies the angular emission pattern. With that goal in mind, we concentrate on the A parameter in Eq. (1) to estimate how the tilt angle Θ affects photoemission probabilities in different setups. For infinitely long IR fields, the A parameter is nothing but the zeroth-order Fourier series coefficient for the periodic dependence of the sideband signal on the delay τ. Therefore, it is a robust (almost time-independent) measure of the differential photoelectron emission probabilities.

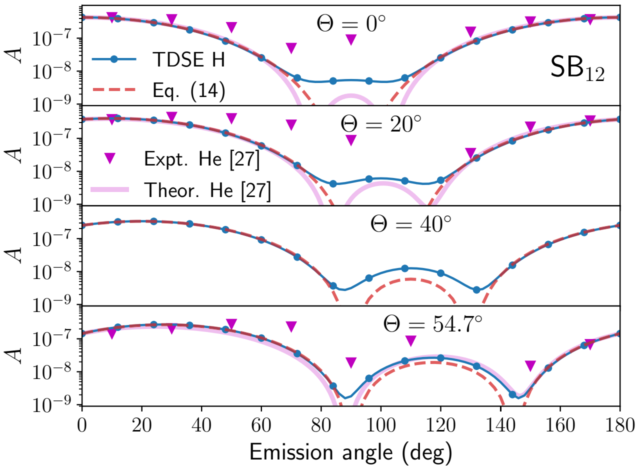

FIG. 4. Time-delay-independent photoelectron emission probabilities [A term in Eq. (1)] as a function of photoelectron emission angle θ for different relative polarization angles Θ between the XUV and the IR fields. Theoretical and experimental data for helium were taken from Ref. [27].

In Fig. 4 we show the dependence of the A parameter on the photoelectron emission angle θ for different pump-probe relative polarization angles. The solid line and circles represent the results we obtain by fitting angle-resolved photoelectron spectra from TDSE simulations with Eq. (1). The data unambiguously show a signal decrease for electron emission in directions perpendicular to the polarization vectors of XUV or IR laser fields. The trend becomes apparent for increasing relative polarization angles Θ, with deeper minima in the signal. The photoelectron emission probabilities span two orders of magnitude and explain the difficulties in the detection, particularly for emission directions where atomic time-delay minima arise. Again, we compare our results with the theoretical and experimental data available [27]. From a qualitative point of view, the experimental results suggest the same pattern we find for minima. Quantitative agreement is only obtained for electron emission directions where probabilities are larger, which exemplifies the difficulties posed by the detection of signals spanning one or more orders of magnitude. The agreement with theoretical data is much more satisfying. Differences in the depth of the wells of photoelectron emission probabilities may stem from the IR pulse setups. In our simulations, the full width at half maximum pulse duration for the IR is about half that considered in Ref. [27] and at the same time the envelopes are different. These two properties are known to induce differences on the Fourier transform of the IR that in turn may influence the numerical values obtained around minima in the observables.

To further understand this behavior, we again resort to analytic tools. Based on the soft-photon approximation [42], it is possible to show that the angular dependence of the nonoscillatory factor A in Eq. (1) is proportional to $\cos^4\theta$ in the parallel ($\Theta = 0^\circ$) case [28]. This result is formally valid for asymptotically high photoelectron energies. However, it describes the angular dependence of A for ε_{k_e} values above a few eV [28,43]. In the following, we derive an analogous expression valid for the nonparallel case. In Refs. [44,45] we model the sideband photoelectron angular distributions for different RABBITT-like configurations as

$$I_{2q}(\theta, \phi) \propto [1 + \beta P_2(\cos\theta)] \sin^2\left(\frac{\mathbf{k}_e \cdot \mathbf{R}}{2}\right), \tag{13}$$

with β the asymmetry parameter for the single-photon ionization of the atomic target by the XUV pulse (pump stage), $P_2(x)$ the second-order Legendre polynomial, $\mathbf{k}_e$ the photoelectron momentum, and $\mathbf{R}$ a vector quantity collinear to the IR polarization direction (see Refs. [44,45] for further details). At variance with more standard approaches like Eq. (1), the equation above remains valid for IR intensities such that continuum-continuum transitions beyond first-order significantly contribute to sideband signals. For usual RABBITT setups, with only lowest-order continuum-continuum channels effectively open, the relation $|\mathbf{k}_e \cdot \mathbf{R}| \ll 1$ holds and the rightmost factor in Eq. (13) can be approximated by $\sin^2(x) \sim x^2$. In addition, as we are analyzing electron emission in the plane defined by the XUV and IR polarization vectors, the scalar product $\mathbf{k}_e \cdot \mathbf{R}$ reduces to $k_e R\,(\cos\theta\cos\Theta + \sin\theta\sin\Theta) = k_e R\cos(\theta - \Theta)$. With these results in mind and provided $\beta = 2$ for initial s states, it is straightforward to show that the angular dependence of the A parameter in Eq. (1) reads

$$A \propto \cos^2\theta \cos^2(\theta - \Theta) \tag{14}$$

for every Θ value and it recovers the $\cos^4\theta$ law for a parallel configuration of the fields.

The direct comparison between the asymptotic model in Eq. (14) (red dashed line) and TDSE simulations in Fig. 4 highlights several facets of the process. First, the angular algebra largely dictates the salient features of photoelectron emission probability. Thus, we expect a universal character for the A parameter provided the initial atomic state has the same angular quantum numbers. Second, the enhanced predictive power of Eq. (14) for Θ approaching 90° brings to the fore the fact that only d partial waves survive for such a configuration [26,40]. Therefore, the s partial wave depletion makes the unbalance of radial matrix elements play a diminishing role. Such an arrangement of laser fields represents the best opportunities for prediction models based on the soft-photon approximation, as they cannot account for relative variations in the weight of each partial wave. In turn, deviations in Fig. 4 between the TDSE results and those from Eq. (14) also stem from small phase shifts between partial waves. However, the model and TDSE calculations differ for photoelectron emission directions whose probabilities are so low that their detection, with current experimental capabilities, could represent a challenge. This fact renders soft-photon approximation models an ideal candidate for quickly assessing some gross features in angularly resolved two-color reaction processes.

IV. CONCLUSION AND OUTLOOK

A simple analytical model was presented in order to predict angularly resolved photoionization time delays in atomic targets employing the RABBITT technique with different relative polarization angles between the XUV and the IR fields. The model reproduced the significant variation of the time delays with the photoelectron angle emission in H and He atoms, revealing a clear phase jump at around 65°, discussed in previous works [17,19,28]. This jump is associated with the relative contribution of different partial waves. Our analytical model perfectly reproduces this behavior. It was demonstrated in hydrogenic atoms and compared with previous theoretical and experimental data for a standard RABBITT scheme, i.e., with collinear fields. More interestingly, we further analyzed the case of different relative polarization angles and compared our results with the available theoretical and experimental data.

First, it was found that it is possible to manipulate the angular dependence of relative time delays by varying the polarization angle between the fields. Indeed, a characteristic double-well shape was found for the time delays as a function of this angle. In other words, a set of phase jump angles was found for noncollinear fields. We explicitly showed that radial matrix elements of emission pathways dictate the photoelectron emission angles for which this family of phase jumps occurs. Furthermore, we demonstrated that phase jumps associated with emission pathways are forbidden only for parallel orientation of the XUV and IR polarization vectors. For any other relative polarization angle between the XUV and IR fields, it should be possible to observe the double-well structure. However, for sufficiently high photoelectron kinetic energy, its observation may be hindered by the shrinking of the characteristic width of each well, which in turn can be predicted from the dependence of radial matrix elements (quotient) on the kinetic energy. Based on this, we can conclude that the ability to guide the position of phase jumps via polarization control allows us to predictably adjust the response time of electrons between the two levels that naturally arise in these systems.

Then we studied the angular dependence of the fitting parameter A characterizing photoelectron emission probabilities in RABBITT sidebands. Taking advantage of previous studies, we put forward an asymptotic law able to predict the behavior of this fitting parameter with reasonably good accuracy. In turn, this simple asymptotic law showed the deep connection between time-delay minima for electron emission directions perpendicular to either the XUV or the IR laser fields and the angular degrees of freedom of the system.

Finally, we want to point out that our analytic model admits an extension to study angular variations of time delays on more complex atomic (or even molecular) targets. That goal can be achieved provided single-center expansions for bound-continuum dipole matrix elements are available. Care should be taken when selecting the method to describe the pump stage of the reaction for other initial states. Noble-gas atoms may display effects such as Cooper minima [46], which should be correctly described by the method of choice in order to ensure an appropriate level of accuracy [47]. We expect this study may foster renewed experimental and theoretical efforts to understand the information conveyed by these observables and eventually use that knowledge to control their behavior.

ACKNOWLEDGMENTS

D.I.R.B., L.M., and O.A.F. acknowledge financial support from the Agencia Nacional de Promoción Científica y Tecnológica, Project PICT No. 01912 (Grant No. 2015-3392), and from the Consejo Nacional de Investigaciones Científicas y Técnicas de la República Argentina, Project PIP No. 3245 (Grant No. 11220200103245). A.P. acknowledges funding from the PRICIT Program from Comunidad de Madrid (Grant No. PCD-I3PCD026 UAM) and Project No. FIS2017-92382-EXP from the Ministerio de Economía y Competitividad (Spain). Part of the results presented in this paper have been obtained using the facilities of the CCT-Rosario Computational Center, a member of the High Performance Computing National System (SNCAD, MINCYT, Argentina).

APPENDIX: EXPANSION COEFFICIENTS $g_{L,L'}$

In this Appendix we explicitly write the coefficients $g_{L,L'}$ for the double summation in Eq. (7) defining the oscillatory pattern of sidebands. The same set of factors enter Eq. (8), from which we extract the time delay τ_{at}. As we solve the TDSE with the QPROP code and it allows us to set noncollinear fields only if their polarization vectors lie in the xy plane, these results are obtained for that configuration of the fields. In addition, as we consider emission into the plane xy defined by the polarization vectors of the XUV and IR radiation fields, the following results are specialized for that case:

$$g_{0,0} = \tfrac{1}{2}\cos^2\Theta, \tag{A1}$$

$$g_{0,2} = \tfrac{1}{4}\cos\Theta[\cos\Theta + 3\cos(\Theta - 2\theta)], \tag{A2}$$

$$g_{2,0} = g_{0,2}, \tag{A3}$$

$$\begin{aligned} g_{2,2} = {} & \tfrac{1}{8}\cos\Theta[\cos\Theta + 6\cos(\Theta - 2\theta)] \\ & + \tfrac{9}{16}[1 + \cos(2\Theta - 4\theta)]. \end{aligned} \tag{A4}$$

Using these expressions for $g_{L,L'}$, it is possible to obtain the angularly resolved time delays from Eq. (8) by replacing the radial matrix elements obtained from SOPT or ACC-RME calculations.

---

[1] R. Pazourek, S. Nagele, and J. Burgdörfer, Attosecond chronoscopy of photoemission, Rev. Mod. Phys. **87**, 765 (2015).

[2] M. Hentschel, R. Kienberger, C. Spielmann, G. A. Reider, N. Milosevic, T. Brabec, P. Corkum, U. Heinzmann, M. Drescher, and F. Krausz, Attosecond metrology, Nature (London) **414**, 509 (2001).

[3] V. Véniard, R. Taïeb, and A. Maquet, Phase dependence of $(N+1)$-color $(N>1)$ ir-uv photoionization of atoms with higher harmonics, Phys. Rev. A **54**, 721 (1996).

[4] P. M. Paul, E. S. Toma, P. Breger, G. Mullot, F. Augé, P. Balcou, H. G. Muller, and P. Agostini, Observation of a train of attosecond pulses from high harmonic generation, Science **292**, 1689 (2001).

[5] C. de Carvalho and H. Nussenzveig, Time delay, Phys. Rep. **364**, 83 (2002).

[6] A. L. Cavalieri, N. Müller, T. Uphues, V. S. Yakovlev, A. Baltuška, B. Horvath, B. Schmidt, L. Blümel, R. Holzwarth, S. Hendel, M. Drescher, U. Kleineberg, P. M. Echenique, R. Kienberger, F. Krausz, and U. Heinzmann, Attosecond spectroscopy in condensed matter, Nature (London) **449**, 1029 (2007).

[7] M. Schultze, M. Fieß, N. Karpowicz, J. Gagnon, M. Korbman, M. Hofstetter, S. Neppl, A. L. Cavalieri, Y. Komninos, T. Mercouris, C. A. Nicolaides, R. Pazourek, S. Nagele, J. Feist, J. Burgdörfer, A. M. Azzeer, R. Ernstorfer, R. Kienberger, U. Kleineberg, E. Goulielmakis *et al.*, Delay in photoemission, Science **328**, 1658 (2010).

[8] K. Klünder, J. M. Dahlström, M. Gisselbrecht, T. Fordell, M. Swoboda, D. Guénot, P. Johnsson, J. Caillat, J. Mauritsson, A. Maquet, R. Taïeb, and A. L'Huillier, Probing Single-Photon Ionization on the Attosecond Time Scale, Phys. Rev. Lett. **106**, 143002 (2011).

[9] M. Froissart, M. L. Goldberger, and K. M. Watson, Spatial separation of events in S-matrix theory, Phys. Rev. **131**, 2820 (1963).

[10] R. Pazourek, S. Nagele, and J. Burgdörfer, Time-resolved photoemission on the attosecond scale: Opportunities and challenges, Faraday Discuss. **163**, 353 (2013).

[11] S. Nagele, R. Pazourek, J. Feist, K. Doblhoff-Dier, C. Lemell, K. Tőkési, and J. Burgdörfer, Time-resolved photoemission by attosecond streaking: Extraction of time information, J. Phys. B **44**, 081001 (2011).

[12] J. Dahlström, D. Guénot, K. Klünder, M. Gisselbrecht, J. Mauritsson, A. L'Huillier, A. Maquet, and R. Taïeb, Theory of attosecond delays in laser-assisted photoionization, Chem. Phys. **414**, 53 (2013).

[13] C. Palatchi, J. M. Dahlström, A. S. Kheifets, I. A. Ivanov, D. M. Canaday, P. Agostini, and L. F. DiMauro, Atomic delay in helium, neon, argon and krypton, J. Phys. B **47**, 245003 (2014).

[14] D. Guénot, D. Kroon, E. Balogh, E. W. Larsen, M. Kotur, M. Miranda, T. Fordell, P. Johnsson, J. Mauritsson, M. Gisselbrecht, K. Varjù, C. L. Arnold, T. Carette, A. S. Kheifets, E. Lindroth, A. L'Huillier, and J. M. Dahlström, Measurements of relative photoemission time delays in noble gas atoms, J. Phys. B **47**, 245602 (2014).

[15] M. Huppert, I. Jordan, D. Baykusheva, A. von Conta, and H. J. Wörner, Attosecond Delays in Molecular Photoionization, Phys. Rev. Lett. **117**, 093001 (2016).

[16] D. Baykusheva and H. J. Wörner, Theory of attosecond delays in molecular photoionization, J. Chem. Phys. **146**, 124306 (2017).

[17] S. Heuser, A. Jiménez Galán, C. Cirelli, C. Marante, M. Sabbar, R. Boge, M. Lucchini, L. Gallmann, I. Ivanov, A. S. Kheifets, J. M. Dahlström, E. Lindroth, L. Argenti, F. Martín, and U. Keller, Angular dependence of photoemission time delay in helium, Phys. Rev. A **94**, 063409 (2016).

[18] C. Cirelli, C. Marante, S. Heuser, C. L. M. Petersson, Á. J. Galán, L. Argenti, S. Zhong, D. Busto, M. Isinger, S. Nandi, S. Maclot, L. Rading, P. Johnsson, M. Gisselbrecht, M. Lucchini, L. Gallmann, J. M. Dahlström, E. Lindroth, A. L'Huillier, F. Martín *et al.*, Anisotropic photoemission time delays close to a Fano resonance, Nat. Commun. **9**, 955 (2018).

[19] D. Busto, J. Vinbladh, S. Zhong, M. Isinger, S. Nandi, S. Maclot, P. Johnsson, M. Gisselbrecht, A. L'Huillier, E. Lindroth, and J. M. Dahlström, Fano's Propensity Rule in Angle-Resolved Attosecond Pump-Probe Photoionization, Phys. Rev. Lett. **123**, 133201 (2019).

[20] A. Autuori, D. Platzer, M. Lejman, G. Gallician, L. Maëder, A. Covolo, L. Bosse, M. Dalui, D. Bresteau, J.-F. Hergott, O. Tcherbakoff, H. J. B. Marroux, V. Loriot, F. Lépine, L. Poisson, R. Taïeb, J. Caillat, and P. Salières, Anisotropic dynamics of two-photon ionization: An attosecond movie of photoemission, Sci. Adv. **8**, eabl7594 (2022).

[21] J. Vos, L. Cattaneo, S. Patchkovskii, T. Zimmermann, C. Cirelli, M. Lucchini, A. Kheifets, A. S. Landsman, and U. Keller, Orientation-dependent stereo Wigner time delay and electron localization in a small molecule, Science **360**, 1326 (2018).

[22] S. Nandi, E. Plésiat, S. Zhong, A. Palacios, D. Busto, M. Isinger, L. Neoričić, C. L. Arnold, R. J. Squibb, R. Feifel, P. Decleva, A. L'Huillier, F. Martín, and M. Gisselbrecht, Attosecond timing of electron emission from a molecular shape resonance, Sci. Adv. **6**, eaba7762 (2020).

[23] F. Holzmeier, J. Joseph, J. C. Houver, M. Lebech, D. Dowek, and R. R. Lucchese, Influence of shape resonances on the angular dependence of molecular photoionization delays, Nat. Commun. **12**, 7343 (2021).

[24] H. Ahmadi, E. Plésiat, M. Moioli, F. Frassetto, L. Poletto, P. Decleva, C. D. Schröter, T. Pfeifer, R. Moshammer, A. Palacios, F. Martin, and G. Sansone, Attosecond photoionisation time delays reveal the anisotropy of the molecular potential in the recoil frame, Nat. Commun. **13**, 1242 (2022).

[25] P. O'Keeffe, R. López-Martens, J. Mauritsson, A. Johansson, A. L'Huillier, V. Véniard, R. Taïeb, A. Maquet, and M. Meyer, Polarization effects in two-photon nonresonant ionization of argon with extreme-ultraviolet and infrared femtosecond pulses, Phys. Rev. A **69**, 051401(R) (2004).

[26] M. Meyer, D. Cubaynes, D. Glijer, J. Dardis, P. Hayden, P. Hough, V. Richardson, E. T. Kennedy, J. T. Costello, P. Radcliffe, S. Düsterer, A. Azima, W. B. Li, H. Redlin, J. Feldhaus, R. Taïeb, A. Maquet, A. N. Grum-Grzhimailo, E. V. Gryzlova, and S. I. Strakhova, Polarization Control in Two-Color Above-Threshold Ionization of Atomic Helium, Phys. Rev. Lett. **101**, 193002 (2008).

[27] W. Jiang, G. S. J. Armstrong, J. Tong, Y. Xu, Z. Zuo, J. Qiang, P. Lu, D. D. A. Clarke, J. Benda, A. Fleischer, H. Ni, K. Ueda, H. W. van der Hart, A. C. Brown, X. Gong, and J. Wu, Atomic partial wave meter by attosecond coincidence metrology, Nat. Commun. **13**, 5072 (2022).

[28] I. A. Ivanov and A. S. Kheifets, Angle-dependent time delay in two-color XUV + IR photoemission of He and Ne, Phys. Rev. A **96**, 013408 (2017).

[29] P. Hockett, Angle-resolved RABBITT: Theory and numerics, J. Phys. B **50**, 154002 (2017).

[30] J. Fuchs, N. Douguet, S. Donsa, F. Martin, J. Burgdörfer, L. Argenti, L. Cattaneo, and U. Keller, Time delays from one-photon transitions in the continuum, Optica **7**, 154 (2020).

[31] K. L. Reid, Photoelectron angular distributions, Annu. Rev. Phys. Chem. **54**, 397 (2003).

[32] C. Joachain, *Quantum Collision Theory* (North-Holland, Amsterdam, 1975).

[33] D. I. R. Boll, L. Martini, and O. A. Fojón, Analytical model for attosecond time delays and Fano's propensity rules in the continuum, Phys. Rev. A **106**, 023116 (2022).

[34] E. W. Weisstein, Harmonic addition theorem, MathWorld—A Wolfram Web Resource, available at https://mathworld.wolfram.com/HarmonicAdditionTheorem.html (Wolfram Research, Champaign).

[35] D. I. R. Boll, O. A. Fojón, C. W. McCurdy, and A. Palacios, Angularly resolved two-photon above-threshold ionization of helium, Phys. Rev. A **99**, 023416 (2019).

[36] A. Jiménez-Galán, F. Martín, and L. Argenti, Two-photon finite-pulse model for resonant transitions in attosecond experiments, Phys. Rev. A **93**, 023429 (2016).

[37] V. Tulsky and D. Bauer, QPROP with faster calculation of photoelectron spectra, Comput. Phys. Commun. **251**, 107098 (2020).

[38] A. P. Jayadevan and R. B. Thayyullathil, Two-photon ionization of atomic hydrogen above the one-photon ionization threshold, J. Phys. B **34**, 699 (2001).

[39] D. I. R. Boll, L. Martini, A. Palacios, and O. A. Fojón, Angularly resolved atomic time delays, Consejo Nacional de Investigaciones Científicas y Técnicas. (dataset), http://hdl.handle.net/11336/182388.

[40] D. I. R. Boll, L. Martini, O. A. Fojón, and A. Palacios, Off-resonance-enhanced polarization control in two-color atomic ionization, Phys. Rev. A **101**, 013428 (2020).

[41] A. S. Kheifets, Symmetry analysis of the photoelectron continuum in two-photon XUV + IR ionization, Phys. Rev. A **105**, 013114 (2022).

[42] A. Maquet and R. Taïeb, Two-colour IR + XUV spectroscopies: The "soft-photon approximation", J. Mod. Opt. **54**, 1847 (2007).

[43] Y. J. Picard, B. Manschwetus, M. Géléoc, M. Böttcher, E. M. S. Casagrande, N. Lin, T. Ruchon, B. Carré, J.-F. Hergott, F. Lepetit, R. Taïeb, A. Maquet, and A. Huetz, Attosecond evolution of energy- and angle-resolved photoemission spectra in two-color (XUV + IR) ionization of rare gases, Phys. Rev. A **89**, 031401(R) (2014).

[44] D. I. R. Boll and O. A. Fojón, Atomic RABBITT-like experiments framed as diatomic molecules, J. Phys. B **49**, 185601 (2016).

[45] D. I. R. Boll and O. A. Fojón, Attosecond polarization control in atomic RABBITT-like experiments assisted by a circularly polarized laser, J. Phys. B **50**, 235604 (2017).

[46] A. S. Kheifets, D. Toffoli, and P. Decleva, Angular dependent time delay near correlation induced cooper minima, J. Phys. B **53**, 115201 (2020).

[47] A. W. Bray, F. Naseem, and A. S. Kheifets, Simulation of angular-resolved RABBITT measurements in noble-gas atoms, Phys. Rev. A **97**, 063404 (2018).